Hybrid CFD-BEM and Time-Reversal techniques applied to localise flow-induced noise sources generated by a flat-plate

Akhilesh Mimani, Paul Croaker, Mahmoud Karimi, Con J. Doolan and Nicole Kessissoglou

School of Mechanical and Manufacturing Engineering, UNSW Australia, Sydney NSW 2052, Australia

ABSTRACT

This paper presents a computational analysis of the flow-induced noise generated by a sharp-edged symmetric flat-plate located in low Mach number flow using the hybrid computational fluid dynamics (CFD)-boundary element method (BEM) and the Time-Reversal (TR) source localisation techniques. The CFD-BEM method is used to obtain the far-field acoustic spectrum of (1) the direct field generated by the turbulent flow over the flat-plate, (2) the acoustic field scattered by the body and (3) the total acoustic field at all four computational boundaries. The far-field acoustic spectrum for all three cases exhibits a broadband nature whereby the time-domain acoustic pressure data is obtained using the inverse Fast Fourier Transform followed by band-passing the signals in 1/3rd octave bands. The aeroacoustic TR simulations were implemented by numerically solving a set of 2-D Linearised Euler Equations and enforcing the band-passed time-reversed acoustic pressure signals as input at the boundary nodes. The TR source maps corresponding to the direct field indicates a lateral quadrupole source located downstream of the Trailing-Edge (TE) in the low-frequency range and a dominant longitudinal quadrupole located at the Leading-Edge (LE) in the high-frequency range. For both scattered and total fields, the TR source maps indicate a lift-dipole source at the TE in the low-frequency range whilst in the high-frequency range, the source maps indicate the occurrence of a weaker dipole source at the LE and a dominant dipole source at the TE.

1. INTRODUCTION

Trailing Edge (TE) noise is produced when boundary-layer turbulence convects past a sharp TE (Blake, 1986). The TE noise is important to a diverse range of engineering applications; a majority of such studies focus on high Reynolds number application such as commercial aircraft, compressors and turbo-machinery, and wind-turbines. However, an experimental analysis of the turbulent boundary-layer noise generated by sharp-edged TE at low-to-moderate Reynolds number (less than half-a-million) has been the subject matter of recent papers (Moreau *et al*., 2012). The motivation behind these investigations is to understand flow-induced noise generated from applications such as micro-wind-turbines, unmanned air vehicles, and underwater control surfaces. In these papers, the mean and unsteady velocity data in the wake and upstream of the TE of a sharp-edged flat-plate were measured using hot-wire anemometry method. The near-field hydrodynamic field data was then related to the far-field acoustic spectra for identifying the flow mechanisms responsible for the TE noise in each flow regime. The flow and noise data was also used to evaluate existing as well as derive new semi-empirical surface pressure spectrum to predict the far-field TE noise generated by the flat-plate model at low-to-moderate Reynolds number (based on the chord).

In addition to the aforementioned approach, the acoustic beamforming method has been popularly used to explicitly identify noise generating regions near the TE (Moreau *et al.*, 2014). The beamforming source maps yield a knowledge of the location of flow-induced sources and the far-field directivity. An alternative array processing technique is the time-reversal (TR) source localisation which has been used to localise experimental aeroacoustic sources in a wind tunnel generated by the Aeolian tone (Mimani *et al*., 2016) and those produced by low Mach number flow over a sharp-edged flat-plate (Mimani *et al*., 2015a). The flat-plate model and the Reynolds number range considered in (Mimani *et al*., 2015a) were the same as those considered by (Moreau *et al*., 2012). It was shown through TR simulations that beyond the low-frequency range, the predicted location of the flow-induced lift-dipole is near the TE; indeed, at high frequencies, the TR source maps indicated the existence of a dominant TE dipole and a significantly weaker LE dipole. Although the TR source maps provided a significant insight into the flow-physics, the limiting feature of this experimental approach was that the microphones cannot separately record the direct field radiated by the turbulent noise sources in the wake of TE and the field scattered by the flat-plate. Rather, the line arrays record the total acoustic field which is the sum of the direct and scattered fields; therefore, the experimental approach cannot separately analyse the source nature of the direct and scattered fields.

The hybrid computational fluid dynamics (CFD)-boundary element method (BEM) developed previously by the authors (Croaker *et al*., 2016), however, enables one to obtain the direct and scattered fields separately, within a computational framework. In view of the limitations of the experimental approach, the authors recently combined the CFD-BEM with the TR method to analyse in detail, the flow-induced noise sources generated by a cylinder at the Aeolian tone or vortex-shedding frequency. The motivation of this paper is then to apply the novel CFD-BEM-TR computational approach to investigate the flow-induced noise generated by the sharp-edged symmetric flat-plate (Moreau *et al*., 2012) within a computational framework and in isolation of the facility effects that were inherently present in the experimental data. It is anticipated that characterisation of the broadband source nature corresponding to the direct, scattered and total fields will not only provide a greater physical insight but will also assist with interpretation of the previous experimental results (Mimani *et al*., 2015a).

The paper is organised as follows. Section 2 describes the methodology to implement the hybrid CFD-BEM technique on the flat-plate model, presents the acoustic spectra of the far-field components and briefly describes the method to obtain the time history data at the boundaries. Section 3 briefly describes the methodology for implementing TR simulation using a computational aeroacoustics (CAA) algorithm. Section 4 presents the TR source maps corresponding to the far-field components and analyses their respective source nature. The important findings of this investigation are then summarised in Section 5.

2. HYBRID CFD-BEM: METHODOLOGY AND RESULTS

A hybrid CFD-BEM technique is used to predict the flow-induced noise generated by turbulent flow past a flat-plate. This technique involves the following steps:

1. A CFD analysis using Large Eddy Simulation (LES) is used to predict the unsteady turbulent flow-field around the flat-plate and to extract the flow-induced noise sources based on the Lighthill's acoustic analogy (Lighthill, 1952);
2. The propagation of the acoustic waves generated by the flow-induced noise sources and prediction of the near-field pressure and pressure gradient incident on the plate;
3. Application of the incident field to a BEM model of the plate based on the Burton-Miller formulation (Burton and Miller, 1971) and calculation of the resulting far-field acoustic pressure. The far-field acoustic pressure is recorded at the data recovery nodes corresponding to the boundary nodes of the TR mesh.

2.1 Hydrodynamic simulation

The sharp-edged full-span symmetric flat-plate (henceforth, referred simply as the flat-plate) considered in the experiments conducted by (Moreau *et al*., 2012) in an Anechoic Wind Tunnel (AWT) was modelled during LES. The flat-plate has a chord length of 200 mm, a span of 450 mm, and a thickness of 5 mm. The leading edge (LE) is circular with a diameter of 5 mm and the TE has a symmetric wedge shape with an apex angle of 12 degrees.

Incompressible flow past the flat-plate is simulated at a Reynolds number Re_c = 4.9 x 10^5 (based on chord length) and a Mach number of M = 0.1. The flow is towards the x direction or along the direction of the flat plate. The LES simulation is performed in Fluent on a C-grid domain with nearly 10 million hexahedral cells. The computational domain is extended two chords above and below the plate as well as upstream, and three chords downstream of the plate. A sponge layer extends the computational domain in the downstream direction for an additional two chords as shown in Figure 1. A high mesh density adjacent to the plate and in the wake region is used to accurately resolve the hydrodynamic fluctuations in both the boundary-layer and the wake regions.

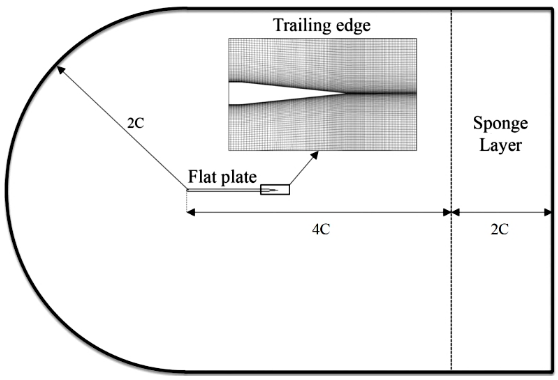

Figure 1: Schematic diagram of the shape and size of the CFD domain.

The inlet velocity is set to 35 m/s on the semi-circular boundary, while a zero average pressure is imposed at the outlet. A no-slip condition is applied on the surface of the plate, and the top and bottom boundaries are considered as free-slip walls. The model is extended 20 mm in the spanwise direction with flow periodicity assumed at the side boundaries.

2.2 Near-field formulation for the flow-induced noise propagation

The propagation of the acoustic waves generated by the flow-induced noise sources to the surface of the flat-plate is resolved using formulations for the near-field pressure and pressure gradient derived based on Lighthill's analogy as developed and described in Croaker *et al.*, 2015. The incident pressure p_a^i and its normal derivative $q_{a,\,n}^i$ on the body are given by

$$p_a^i(\mathbf{x},\,\mu) = \lim_{\epsilon \to 0} \int_{(\Omega - V_\epsilon)} T_{ij}(\mathbf{y},\,\mu) \frac{\partial^2 G_h}{\partial y_i \partial y_j} \mathrm{d}y \tag{1}$$

$$q_{a,\,n}^i(\mathbf{x},\,\mu) = \lim_{\epsilon \to 0} \int_{(\Omega - V_\epsilon)} T_{ij}(\mathbf{y},\,\mu) \frac{\partial^3 G_h}{\partial y_i \partial y_j \partial n} \mathrm{d}y \tag{2}$$

where y_i is the i^{th} component of the acoustic source point position vector **y**. It is noted that **x** is the field point where the near-field pressure and its normal derivative are recovered, Ω is the computational domain and V_ϵ represents an exclusion neighbourhood taken around the field point. This exclusion neighbourhood allows the singularities occurring when **y** = **x** to be regularised. The free-field Green's function of the wave equation is given by

$$G_h = \frac{\mathrm{j}}{4} H_0^1\left(k_a r\right) \tag{3}$$

where $\mathrm{j} = \sqrt{-1}$, the imaginary unit, k_a is the acoustic wavenumber, $H_0^1(.)$ is the Hankel function of the first-kind and zero order (signifying outward propagating cylindrical waves) and $r = |\mathbf{x} - \mathbf{y}|$. Furthermore, T_{ij} is the Lighthill tensor represented by $T_{ij} = {}^\circ{}_0 u_i u_j$, where u_i is the i^{th} component of the velocity vector and ${}^\circ{}_0 = 1.21\ \mathrm{kg \cdot m^{-3}}$ is the density of the fluid. Details of the formulations used for the near-field pressure and pressure gradient and their numerical treatment can be found in (Croaker *et al.*, 2015).

2.3 Scattering of the incident aeroacoustic fields using BEM

The inhomogeneous Helmholtz equation is given by

$$\Delta p_a(x) + k_a^2 p_a = -Q \tag{4}$$

where the inhomogeneity Q is an acoustic source. Applying the Burton-Miller formulation (Burton and Miller, 1971) to Eq. (4) and combining with the incident field (Eqs. (1) and (2)) produced by the aeroacoustic sources yields

$$\begin{aligned} &c(\mathbf{y}) p_a(\mathbf{y}) + \int_\Gamma p_a(\mathbf{x}) \frac{\partial G_h}{\partial n(\mathbf{x})} \mathrm{d}\Gamma + \mathrm{j} \quad \int_\Gamma p_a(\mathbf{x}) \frac{\partial^2 G_h}{\partial n(\mathbf{x}) \partial n(\mathbf{y})} \mathrm{d}\Gamma = \\ &\mathrm{j}\, {}^\circ{}_0 c_0 k_a \left(\int_\Gamma \left(v_a(\mathbf{x}) G_h \right) \mathrm{d}\Gamma - \mathrm{j} \quad \left(c(\mathbf{y}) v_a(\mathbf{y}) - \int_\Gamma v_a(\mathbf{x}) \frac{\partial G_h}{\partial n(\mathbf{y})} \mathrm{d}\Gamma \right) \right) + p_a^i(\mathbf{y}) + \mathrm{j} \quad q_a^i(\mathbf{y}) \end{aligned} \tag{5}$$

where $c(\mathbf{y})$ is a free-term coefficient and equals 1 in the interior domain and 0.5 on a smooth boundary. Furthermore, n is the unit normal to the boundary,   is the Burton and Miller coupling parameter, c_0 = 343 m/s is the sound speed of the fluid medium at rest and v_a is the fluid particle velocity. In this paper, Eq. (5) is solved using the two dimensional AEBEM2 solver of Kirkup which yields the (complex) spectrum of the scattered acoustic far-field (Kirkup, 1998). The sum of the complex far-field spectrum of the direct and scattered fields yields the total acoustic far-field spectrum. The flat-plate is discretised into 100 evenly spaced one-dimensional boundary elements.

2.4 Far-field acoustic pressure spectra at boundaries and converting them to time domain data

The far-field acoustic pressure spectrum of the direct, scattered and total fields generated by the flat-plate in cross-flow were computed on boundaries of the square domain $-0.1525 \text{ m} \le x \le 0.5475 \text{ m}$, $|y| \le 0.35 \text{ m}$. The location of the TE of the plate coincides with the centre of the square domain given by $x = 0.1975 \text{ m}$, $y = 0$. On each side of the square boundary, 201 equally spaced data recovery points were positioned that coincide with the boundary nodes. The mesh-size is given by $\Delta x = \Delta y = 3.5 \text{ mm}$. The spectrum (frequency domain) data of the direct acoustic radiation from the flow-induced noise sources as well as the scattered and total acoustic pressure fields were computed at the 800 boundary nodes or four boundaries which completely encloses the square domain.

Figure 2(a) shows the far-field spectrum of the direct field radiated by the flow-induced noise sources whilst Fig. 2(b) shows the spectrum of the field scattered by it and the total acoustic field. Both parts (a) and (b) show the spectra corresponding to the Welch segment 1 computed at the node $x = 0.096 \text{ m}$, $y = -0.35 \text{ m}$ on the bottom boundary. The spectra shown in Fig. 2 demonstrates the broadband noise characteristics (resembling white-noise) of the direct, scattered and the total fields generated by flow over the sharp-edged symmetric plate (Moreau *et al.*, 2012). As may be noted that the scattered field is approximately 25 dB stronger than the direct field for frequencies up to 1100 Hz and approximately 35 dB stronger at higher frequencies. Thus, the scattered field completely dominates, with the scattered and total field spectra almost co-incident across the frequency range. In this relation, it is noted that direct field corresponds to a quadrupole source (generated in the TE wake) which has low radiation efficiency, while the scattered field generated by the interaction of direct field with the plate corresponds to a dipole source which has a higher radiation efficiency. The acoustic power F_D radiated from the direct field scales as M^8 while the acoustic power F_S radiated from the scattered field scales as M^5, therefore, for $M << 1$, $F_S >> F_D$ which explains the dominance of the scattered field. The spectra of Welch segments 2 to 4 for the direct, scattered and total fields were found to be similar to the Welch segment 1 spectra.

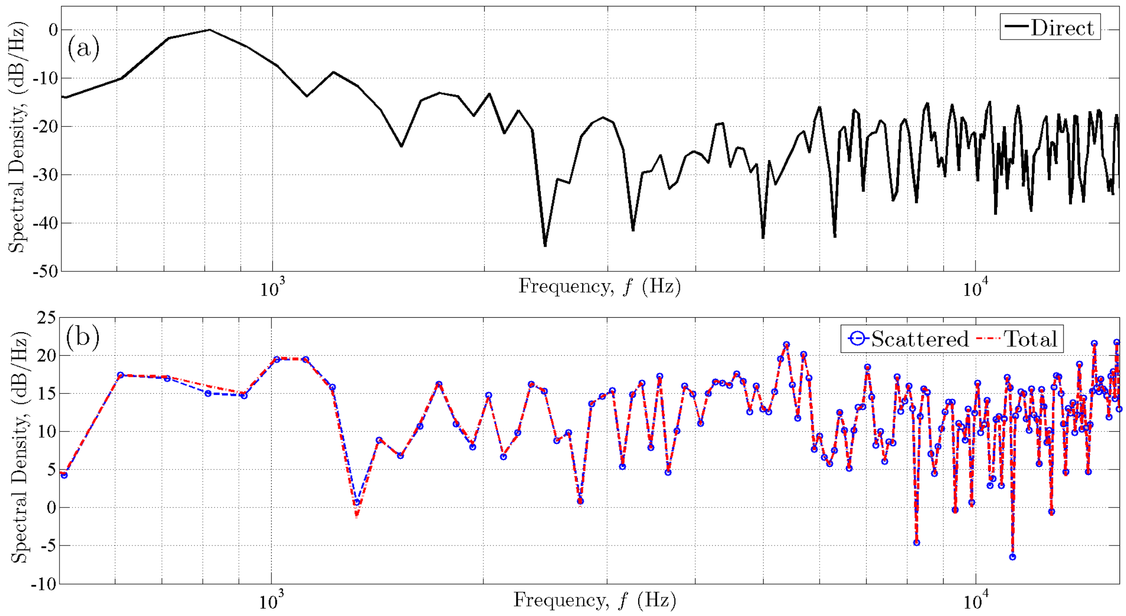

Figure 2: The far-field acoustic spectra of (a) the direct, (b) scattered and total acoustic pressure fields for Welch segment 1 computed numerically using LES at the node $x = 96 \text{ mm}$, $y = 0$ (on the bottom boundary).

The far-field boundary spectra were converted to time domain acoustic pressure signals using inverse Fast Fourier Transform (IFFT) implemented in MATLAB where the NFFT size was equal to 4096 points. The time domain signals were band-pass filtered in different one-third octave bands starting from the lowest band of interest with centre frequency $f_c = 630 \text{ Hz}$ up to the highest band of interest having $f_c = 6300 \text{ Hz}$ whereby the TR simulations were implemented using the band-pass filtered time domain data corresponding to each one-third octave bands.

3. AEROACOUSTIC TIME-REVERSAL (TR) SIMULATION: METHODOLOGY

The TR simulation was implemented by numerically solving the two-dimensional LEE given by Eqs. (6-8) using the Pseudo-Characteristic Formulation (PCF) (Sesterhenn, 2000) on a square-domain $-0.1525 \text{ m} \le x \le 0.5475 \text{ m}$,

$|y| \le 0.35\ \mathrm{m}$ in reverse time $\tilde{t}$ with anechoic boundary conditions and enforcing the time-reversed band-pass filtered acoustic pressure history $\tilde{p}(x, y, \tilde{t})$ at line arrays located at the four boundaries (Mimani *et al.*, 2015b).

$$\begin{aligned}
\frac{\partial \tilde{p}}{\partial \tilde{t}} &= -\frac{{}^{\circ}{}_{0}c_0}{2}\left(\tilde{X}^{+}_{\text{linear}} + \tilde{X}^{-}_{\text{linear}} + \tilde{Y}^{+}_{\text{linear}} + \tilde{Y}^{-}_{\text{linear}}\right) \\
\frac{\partial \tilde{u}}{\partial \tilde{t}} &= -\frac{1}{2}\left(\tilde{X}^{+}_{\text{linear}} - \tilde{X}^{-}_{\text{linear}}\right) - \tilde{v}\left(-\frac{\partial U_\infty}{\partial y}\right) - \left(\tilde{u} + \frac{-U_\infty}{c_0}\frac{\tilde{p}}{{}^{\circ}{}_{0}c_0}\right)\left(-\frac{\partial U_\infty}{\partial x}\right) \\
\frac{\partial \tilde{v}}{\partial \tilde{t}} &= -\frac{1}{2}\left(\tilde{Y}^{+}_{\text{linear}} - \tilde{Y}^{-}_{\text{linear}}\right) - \left(-U_\infty\right)\frac{\partial \tilde{v}}{\partial x}
\end{aligned} \tag{6-8}$$

where $$\tilde{X}^{\pm}_{\text{linear}} = \pm\left(c_0 \mp U_\infty\right)\left(\frac{1}{\rho_0 c_0}\frac{\partial \tilde{p}}{\partial x} \pm \frac{\partial \tilde{u}}{\partial x}\right) \quad \text{and} \quad \tilde{Y}^{\pm}_{\text{linear}} = \pm\, c_0\left(\frac{1}{\rho_0 c_0}\frac{\partial \tilde{p}}{\partial y} \pm \frac{\partial \tilde{v}}{\partial y}\right) \tag{9-12}$$

denote a pair of opposing fluxes propagating towards the *x* and *y* directions, respectively. Furthermore, $\tilde{u}$ and $\tilde{v}$ denote acoustic velocities (m/s) along the *x* and *y* directions, respectively, whilst the free-stream velocity U_∞ is set to zero during TR simulation. The spatial derivative of acoustic pressure and velocities in the opposing fluxes $(\tilde{X}^{\pm}_{\text{linear}}, \tilde{Y}^{\pm}_{\text{linear}})$ of the PCF were computed using an overall upwind-biased Finite-Difference (FD) scheme that is formulated using a fourth-order, seven-point optimised upwind-biased FD scheme at interior nodes and a seven-point optimised backward FD scheme at the boundary nodes. The third-order Total-Variation-Diminishing Runge-Kutta scheme was used for time-integration and as indicated earlier, the $CFL = 0.24$. The instantaneous time-reversed acoustic pressure field $\tilde{p}(x, y, \tilde{t})$ during TR simulations was obtained using the superposition technique in the low-frequency range (up to $f_c = 2000\ \mathrm{Hz}$) and use of Time-Reversal-Sponge-Layer near the line arrays from the frequency band $f_c = 2500\ \mathrm{Hz}$ onwards. This CAA algorithm is presented in a greater detail in (Mimani *et al*. 2015b).

The TR simulation was implemented over the reverse time interval $\tilde{t} = \left[0,\ N_{\max}\Delta t = 4096\Delta t\right]$ whereby the aeroacoustic source location/characteristics were obtained by determining the focal spots in the RMS time-reversed acoustic pressure field (computed when a steady-state field is observed throughout the domain) denoted by $\tilde{p}^{TR}_{RMS}(x, y)$. It is noted that the time-step $\Delta t = 2.4\times10^{-6}$ s taken during TR corresponds to one-fourth of the time-step $\Delta t_{LES} = 9.6\times10^{-6}$ s considered during LES for computing near-field time domain data. (Δt_{LES} corresponds to the sampling frequency $F_s \approx 104167\ \mathrm{Hz}$.) The focal spot maximum is termed the focal point. The $\tilde{p}^{TR}_{RMS}(x, y)$ field was converted to the dB scale (*w.r.t.* $p_{ref} = 2\times10^{-5}$ Pa) and is denoted by $\tilde{p}^{TR}_{\text{dB}}(x, y)$, [Mimani *et al*., 2015b].

4. TIME-REVERSAL SIMULATION RESULTS

The TR source maps due to the direct, scattered and total fields were computed using the time-reversed acoustic pressure signals at the four line arrays corresponding to each Welch segment 1 to 4, following which the average source maps was obtained that are presented in the ensuing subsection.

4.1 Direct acoustic field

Figures 3 and 4 shows the average TR source maps (RMS acoustic pressure field) of the flat-plate over the dynamic range [0, -15 dB] due to the direct acoustic field in different one-third octave frequency bands. Parts (a-f) of Fig. 3 correspond to the centre band frequency $f_C = 630$ Hz, 800 Hz, 1000 Hz, 1250 Hz, 1600 Hz and 2000 Hz, respectively, whilst parts (a-e) of Fig. 4 correspond to $f_C = 2500$ Hz, 3150 Hz, 4000 Hz, 5000 Hz and 6300 Hz, respectively. In Figs. 3 and 4, the flat-plate and the four line arrays (at the boundaries) are shown by white lines; the same symbolic convention and dynamic range are followed in the remaining source maps. In Figs. 3(a-f), the occurrence of four focal spots in the TE wake indicate that the flow-induced turbulent noise due to the direct field generated by the flat-plate has a lateral quadrupole nature (in the low-frequency region) whose axes are inclined at 45° and 135° with respect to the flow direction.

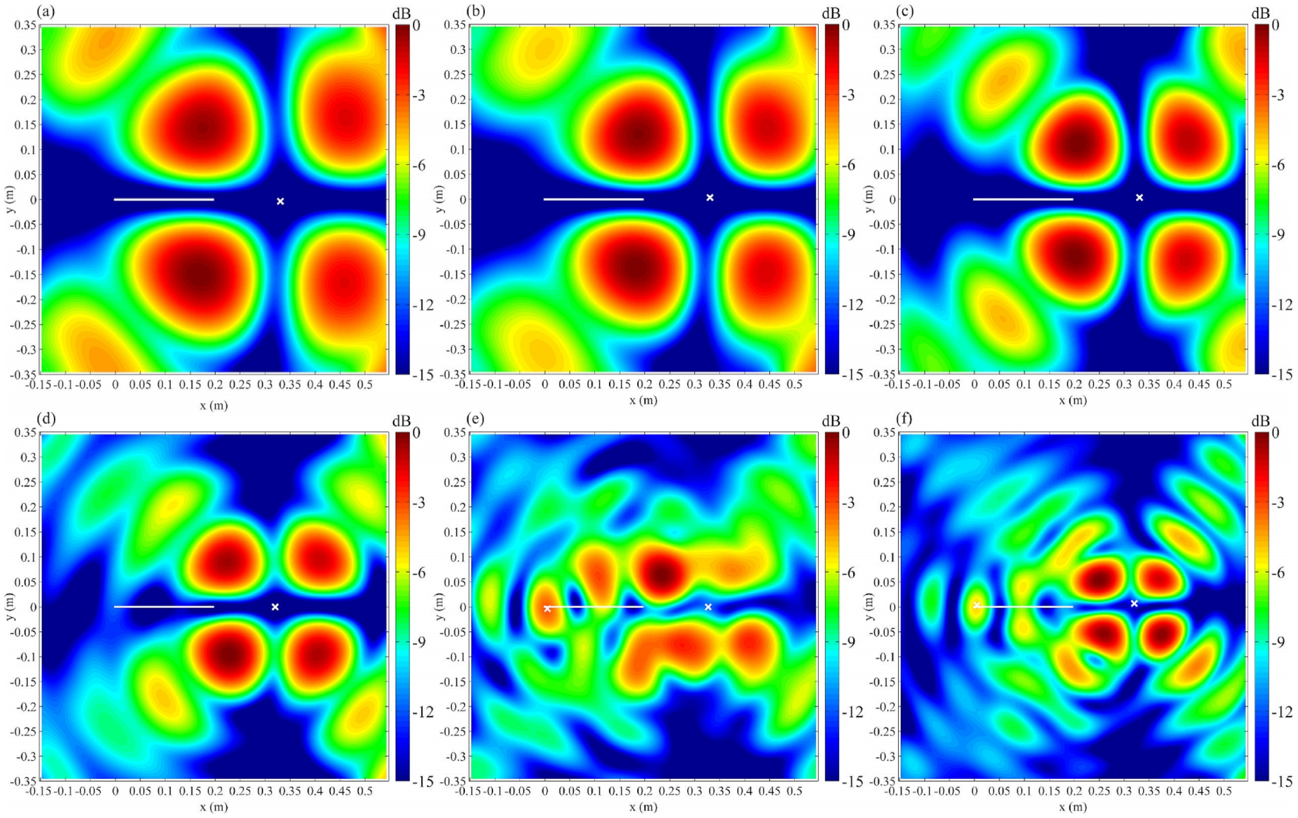

Figure 3: TR source maps due to the direct acoustic field in the one-third octave frequency bands with f_C given by (a) 630 Hz, (b) 800 Hz, (c) 1000 Hz, (d) 1250 Hz, (e) 1600 Hz, (f) 2000 Hz.

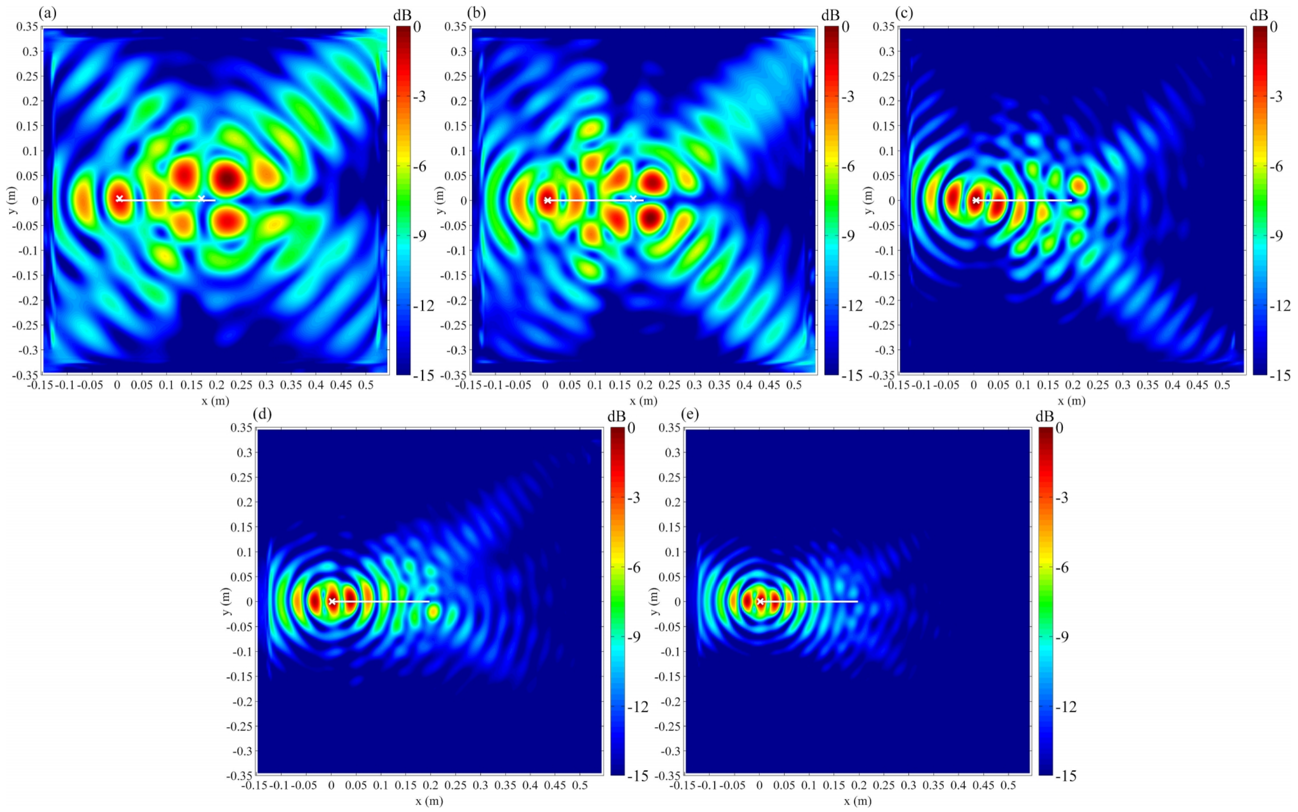

Figure 4: TR source maps due to the direct acoustic field in the one-third octave frequency bands with f_C given by (a) 2500 Hz, (b) 3150 Hz, (c) 4000 Hz, (d) 5000 Hz and (e) 6300 Hz.

The predicted location of the lateral quadrupole source is taken as the geometrical centre of the four focal points and is denoted by a cross **X** in Fig. 3. (The same symbolic convention is followed in the remaining source maps to denote the predicted source location.) It is observed from Figs. 3(a-f) that while the location of the lateral quadrupole source in the LE wake remains constant over different frequency bands, the focal spot size decreases or the resolution improves with frequency (Mimani *et al.*, 2015a, 2016). Of a particular importance is the occurrence of a weaker focal spot near the LE in Figs. 3(e) and (f) which suggests the existence of another (incoherent) source near the TE in these frequency ranges. Further details on the nature of this additional source will be evident from source maps shown in Fig. 4 corresponding to the higher frequency range.

Figures 4(a) and (b) indicate that the LE focal spot is flanked by two weaker focal spots (along the direction of the plate); the strength of the LE focal spot is comparable to the focal spots constituting the lateral quadrupole source whose location is now shifted upstream over a region between the mid-span and the TE of the flat-plate. The pattern of formation of three focal spots near the LE indicates that a longitudinal quadrupole source nature of this additional source. Figure 4(c) indicate the longitudinal quadrupole source at the LE is much stronger than the TE lateral quadrupole source. Figures 4(d) and (e) demonstrate that at $f_C =$ 5000 Hz and 6300 Hz, the LE longitudinal quadrupole source completely dominates and overwhelms the TE lateral quadrupole sources; indeed, it is impossible to see the presence of latter source near the TE. It is for this reason that the location of lateral quadrupole source is not shown in Figs. 4(c-e). The occurrence of a dominant LE longitudinal quadrupole source nature (in high-frequency range) of the direct field generated by the plate can be explained by carrying out a CFD analysis of the hydrodynamic velocity field near the flat plate. It is most likely due to the formation of a separation bubble near the LE whose small size results in the excitation of this source only in the high-frequency range.

4.2 Scattered and total acoustic fields

Figures 5 and 6 shows the average TR source maps of the flat-plate due to the scattered acoustic field in different one-third octave frequency bands. Parts (a-f) of Fig. 5 correspond to centre band frequency $f_C =$ 630 Hz, 800 Hz, 1000 Hz, 1250 Hz, 1600 Hz and 2000 Hz, respectively, whilst parts (a-e) of Fig. 6 correspond to $f_C =$ 2500 Hz, 3150 Hz, 4000 Hz, 5000 Hz and 6300 Hz, respectively. In Fig. 5, the formation of two focal spots on opposite sides of the plate indicates the lift-dipole source nature of the scattered acoustic field. The predicted location of the lift-dipole is taken as the geometrical centre of the two focal spots and is indicated by a cross **X**. Figures 5(a) and (b) show that in the low-frequency range, the dipole source is located in the region between the mid-span and the TE of the plate. With an increase in the frequency band, the dipole location shifts towards the TE of the flat-plate as may be observed from Figs. 5(c-f) and the focal-resolution of the source improves. Of particular interest, is the formation of elongated focal spots in the frequency band $f_C =$ 1000 Hz, these focal spots begins to bifurcate at $f_C =$ 1250 Hz. Figure 5(f) shows that at $f_C =$ 2000 Hz, the bifurcation is complete, characterised by the occurrence of a stronger TE dipole source and an additional (much weaker) dipole near the LE. Parts (a-e) of Fig. 6 demonstrate that the strength (at focal points) of the LE dipole source increases with frequency and it becomes progressively more easily noticeable. (The LE dipole source is denoted by a cross and this convention is also followed in Fig. 8.) However, the relative strength of the LE dipole is less than that of TE dipole for all frequency bands shown in Fig. 6. This result is anticipated as the TE dipole is known to be dominant noise sources at high frequencies (Howe, 1999).

Figures 7 and 8 show the average TR source maps due to the total field in different one-third octave bands. It is observed that Figs. 7(a-f) are identical to Figs. 5(a-f), respectively, whilst Figs. 8(a-e) are identical with Figs. 6(a-e), respectively, thereby demonstrating that the source nature of the total and scattered fields are same. This result is consistent with the far-field spectra shown in Fig. 2 which indicates that magnitude of the scattered field is significantly greater than that of the direct field. Since the scattered field has a lift-dipole source nature at the TE (and LE) and dominates the weaker quadrupole source produced by the direct field, it was anticipated that the TR source map of the total field also has a lift-dipole nature which is indeed observed in Figs. 7 and 8. Furthermore, Figs. 7 and 8 are the simulation-based counterparts of the experimental TR source maps of the flow-induced noise generated by flat-plate in cross-flow presented previously (Mimani *et al.*, 2015a). This is because, during experiments carried out in AWT, the microphones simultaneously intercept both the direct and scattered radiation implying that the total field is recorded. Since the scattered field component dominates the total field, the experimental TR source maps show a lift-dipole nature and are indeed comparable with Figs. 7 and 8 computed using the hybrid CFD-BEM-TR method.

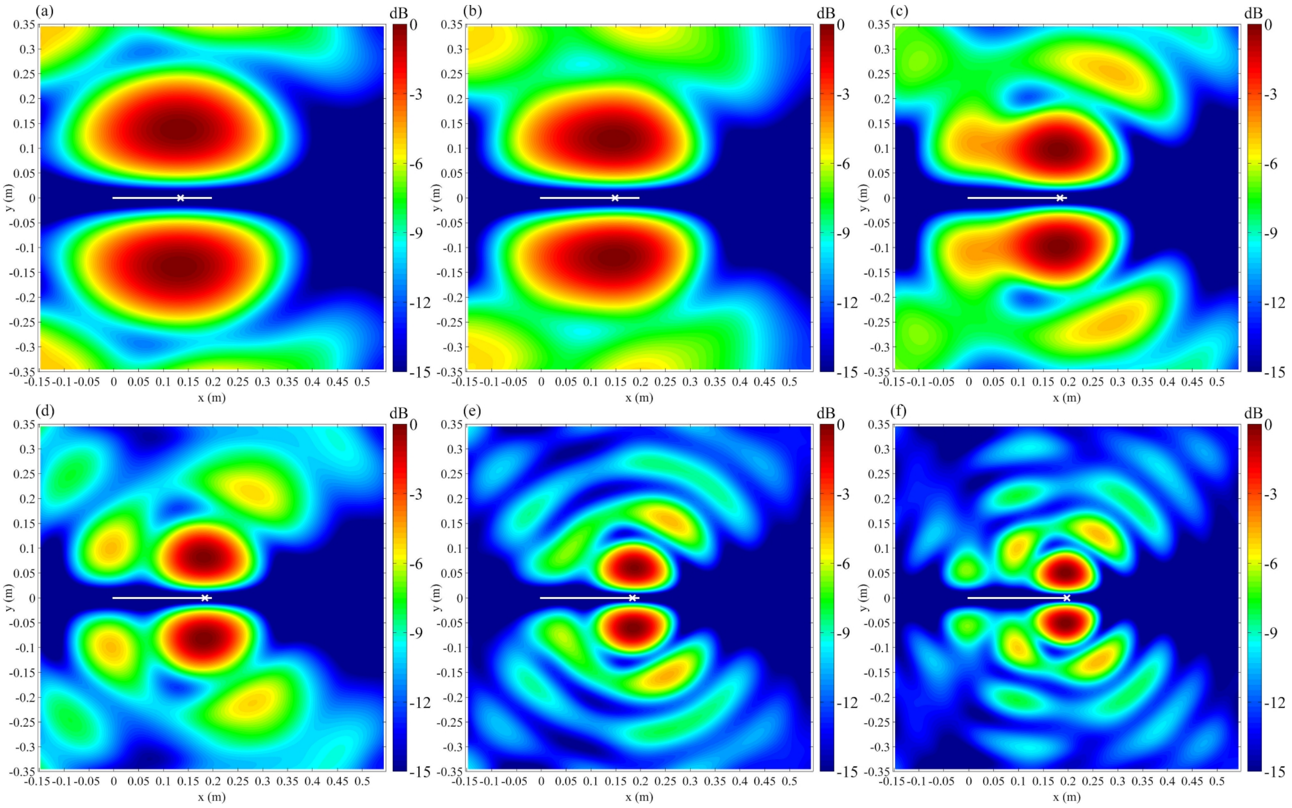

Figure 5: TR source maps due to the scattered acoustic field in the one-third octave frequency bands with f_C given by (a) 630 Hz, (b) 800 Hz, (c) 1000 Hz, (d) 1250 Hz, (e) 1600 Hz, (f) 2000 Hz.

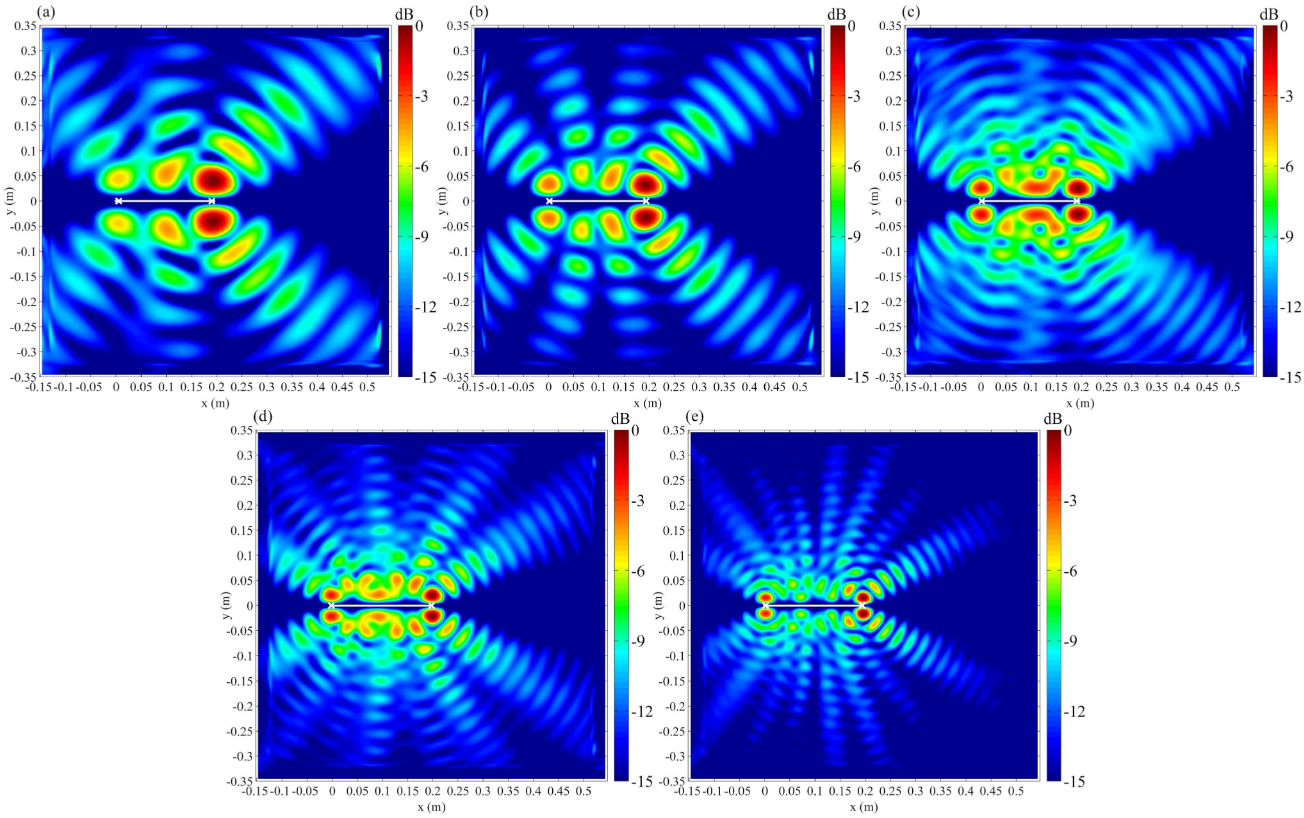

Figure 6: TR source maps due to the scattered acoustic field in the one-third octave frequency bands with f_C given by (a) 2500 Hz, (b) 3150 Hz, (c) 4000 Hz, (d) 5000 Hz and (e) 6300 Hz.

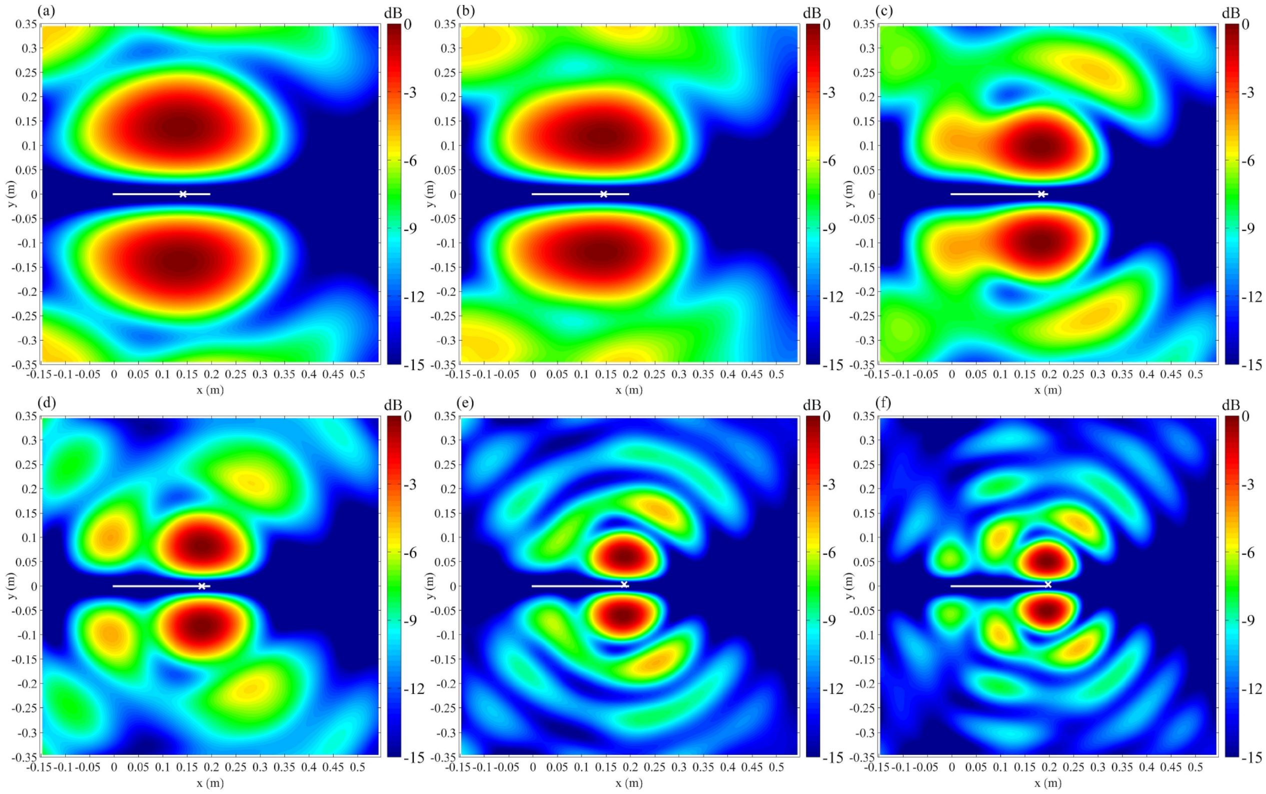

Figure 7: TR source maps due to the total acoustic field in the one-third octave frequency bands with f_C given by (a) 630 Hz, (b) 800 Hz, (c) 1000 Hz, (d) 1250 Hz, (e) 1600 Hz, (f) 2000 Hz.

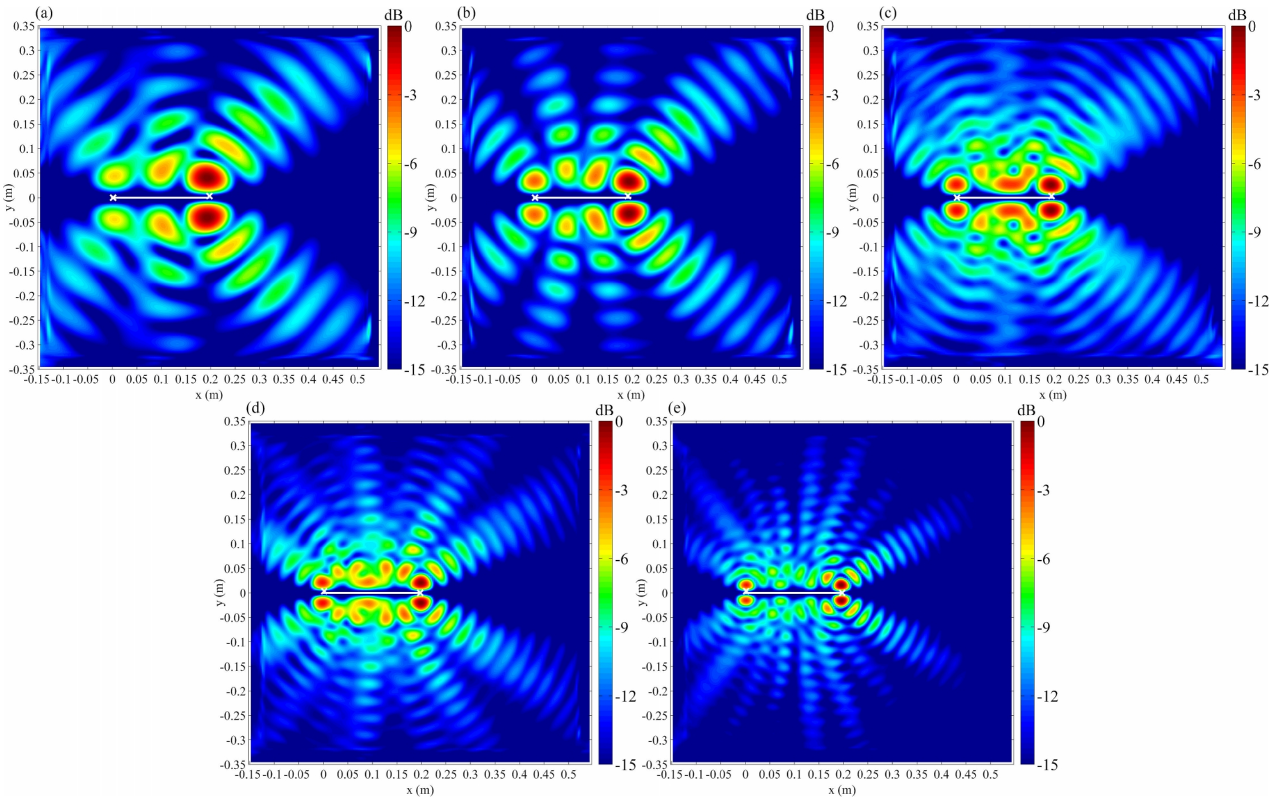

Figure 8: TR source maps due to the total acoustic field in the one-third octave frequency bands with f_C given by (a) 2500 Hz, (b) 3150 Hz, (c) 4000 Hz, (d) 5000 Hz and (e) 6300 Hz.

5. CONCLUSIONS

This paper has presented a combined hybrid CFD-BEM-TR technique to analyse aeroacoustic sources generated by a sharp-edged full-span symmetric flat-plate located in a low Mach number flow. The hybrid CFD-BEM provides the individual far-field acoustic spectra of the direct, scattered and total acoustic fields at all boundary nodes which was then converted to the time domain and used as input during the TR simulation. This enables the computation of the TR source maps of the direct, scattered and total fields separately and thus, analyse their respective source nature which yields a greater physical insight into the flow-induced noise production mechanism of the flat-plate as compared to the previous experimental approach (Mimani *et al*., 2015a). Furthermore, the present simulation-based approach allows TR to investigate noise mechanisms in complete isolation of the facility effects that were inherently present in the experimental data. The TR source maps corresponding to the direct field indicates a lateral quadrupole source located downstream of the TE in the low-frequency range and a dominant longitudinal quadrupole source located at the LE in the high-frequency range. For both scattered and total fields, the TR source maps yield a lift-dipole source at the TE in the low-frequency range whilst in the high-frequency range, the source maps indicate the occurrence of a weaker dipole source at the LE and a dominant dipole source at the TE, thereby corroborating the previous experimental results. A successful demonstration of the hybrid CFD-BEM-TR technique for analysing flow-induced noise produced by a flat-plate suggests that it can be further developed as a diagnostic tool to investigate more complicated test-cases (such as wall-mounted airfoil or cylinder) and may also serve as a useful reference for the interpretation of the corresponding experimental TR results.

REFERENCES

Blake, W 1986, *Mechanics of Flow Induced Sound and Vibration*, vol. II, Academic Press, London.

Burton, AJ & Miller, GF 1971, 'The application of integral equation methods to the numerical solution of some exterior boundary-value problems', *Proceedings of the Royal Society of London. Series A, Mathematical and Physical Sciences*, Vol. 323, pp. 201-210.

Croaker, P, Kessissoglou, N & Marburg, S 2015, 'Strongly singular and hypersingular integrals for aeroacoustic incident fields', *International Journal of Numerical Methods in Fluids*, vol. 77, no. 5, pp. 274-318.

Croaker, P, Kessissoglou, N & Marburg, S 2016, 'Aeroacoustic scattering using a particle accelerated computational fluid dynamics/boundary element technique', *AIAA Journal*, vol. 54, no. 7, pp. 2116-2133.

Howe, M 1999, 'Trailing edge noise at low Mach numbers', *Journal of Sound and Vibration*, vol. 225, no. 2, pp. 211–238.

Kirkup, SM 1998, *The Boundary Element Method in Acoustics, Integrated Sound Software*, Heptonstall, pp. 90-93.

Lighthill, MJ 1952, 'On sound generated aerodynamically, I. General theory', *Proceedings of the Royal Society A*, vol. 211, no. 1107, pp. 564-587.

Mimani, A, Moreau, DJ & Doolan, CJ 2015a, 'Experimental application of aeroacoustic time-reversal', Proceedings of the 21st AIAA/CEAS Aeroacoustics Conference, Dallas, Texas, Paper 3143, pp. 1-19.

Mimani, A, Prime, Z, Doolan, CJ & Medwell, PR 2015b, 'A sponge-layer damping technique for aeroacoustic time-reversal', *Journal of Sound and Vibration*, vol. 342, pp. 124-151.

Mimani, A, Moreau, DJ, Prime, Z & Doolan, CJ 2016, 'An experimental application of aeroacoustic time-reversal to the Aeolian tone', *The Journal of the Acoustical Society of America*, vol. 139, no. 2, pp. 740–763.

Moreau, DJ, Brooks, LA & Doolan, CJ 2012, 'The effect of boundary layer type on trailing edge noise from sharp-edged flat plates at low-to-moderate Reynolds number', *Journal of Sound Vibration*, vol. 331, no. 17, pp. 3976-3988.

Moreau, DJ, Prime, Z, Porteous, R, Doolan, CJ & Valeau, V 2014, 'Flow-induced noise of a wall- mounted finite airfoil at low-to-moderate Reynolds number', *Journal of Sound Vibration*, vol. 333, no. 25, pp. 6924-6941.

Sesterhenn, J 2001, 'A characteristic-type formulation of the Navier-Stokes equations for high order upwind schemes', *Computers and Fluids*, vol. 30, no. 1, pp. 37-67.